RSC Advances

PAPER

View Article Online
View Journal | View Issue

Cite this: *RSC Adv.*, 2021, **11**, 37995

Effect of interfacial defects on the electronic properties of MoS_2 based lateral T–H heterophase junctions†

Mohammad Bahmani, *[a] Mahdi Ghorbani-Asl *[b] and Thomas Frauenheim*[cde]

The coexistence of semiconducting (2H) and metallic (1T) phases of MoS_2 monolayers has further pushed their strong potential for applications in the next generation of electronic devices based on two-dimensional lateral heterojunctions. Structural defects have considerable effects on the properties of these 2D devices. In particular, the interfaces of two phases are often imperfect and may contain numerous vacancies created by phase engineering techniques, *e.g.* under an electron beam. Here, the transport behaviors of the heterojunctions with the existence of point defects are explored by means of first-principles calculations and non-equilibrium Green's function approach. While vacancies in semiconducting MoS_2 act as scattering centers, their presence at the interface improves the flow of the charge carriers. In the case of V_{Mo}, the current has been increased by two orders of magnitude in comparison to the perfect device. The enhancement of transmission was explained by changes in the electronic densities at the T–H interface, which open new transport channels for electron conduction.

Received 8th August 2021
Accepted 5th November 2021

DOI: 10.1039/d1ra06010d

rsc.li/rsc-advances

Among the developing family of two-dimensional (2D) materials, transition metal dichalcogenides (TMDs) provide some of the most diverse electronic properties including acting as topological insulators, semiconductors, (semi)metals and superconductors.[1–3] Noticeably, such a difference in the electronic structure of TMDs correlates with their structural configurations, called phases.[4] Monolayers of MoS_2 in the H-phase, with trigonal prismatic coordination of metal atoms, is a semiconducting material,[5,6] while T-phase with octahedral coordination shows metallic character. The H-phase monolayer is reported to be a promising material for field-effect transistors (FETs) with small-scale channel lengths and negligible current leakage.[5,6]

Recent experiments have already shown controlled transitions from one phase to another *via* external stimuli such as electron beam,[7] ion intercalation,[8] or laser irradiation.[9] These phase-engineered 2D materials with minimum variations in atomic structure and uniform stoichiometry not only demonstrate rich physical behavior but also open up new avenues for the design of electronic devices. The fabrication of lateral metallic/semiconducting heterostructures has been suggested as a practical method to minimize the contact resistance at the interface between 2D semiconductors and metal electrodes. In particular, the formation of covalent bonds between the two phases can introduce paths for carriers to travel across the interfaces, thus, the Schottky barrier and contact resistance are reduced.[10–13] It has also been demonstrated that 1T-phase engineered electrodes in MoS_2 based electronic devices would generate ohmic contacts and, as a result, improve electrical characteristics.[12,14]

Apart from intrinsic defects, the local phase transitions induced by electron beam irradiation may give rise to the formation of point defects, in particular at the interface of the two phases.[15–22] Defects can also be intentionally introduced during the post-growth stage *via* ion bombardment, plasma treatment, vacuum annealing, or chemical etching.[15–22] Indeed, theoretical and experimental results showed that the presence of sulfur vacancies can decrease the energy difference between the H and T phases and eventually stabilize the 1T phase in MoS_2 monolayer.[23,24] The presence of point defects in semiconducting MoS_2 monolayers leads to the observation of the localized states in their electronic structure, which act as short-ranged scattering centers for charge carriers.[25–28] Hence, defects were found to deteriorate the mobility of the fabricated

[a]*Bremen Center for Computational Materials Science (BCCMS), Department of Physics, Bremen University, 28359 Bremen, Germany. E-mail: mbahmani@uni/bremen.de; Tel: +49 421 21862338*

[b]*Institute of Ion Beam Physics and Materials Research, Helmholtz-Zentrum Dresden-Rossendorf, 01328 Dresden, Germany. E-mail: mahdi.ghorbani@hzdr.de; Tel: +49 351 2603613*

[c]*Bremen Center for Computational Materials Science (BCCMS), Department of Physics, Bremen University, 28359 Bremen, Germany. E-mail: thomas.frauenheim@bccms.uni-bremen.de; Tel: +49 421 21862340*

[d]*Beijing Computational Science Research Center (CSRC), 100193 Beijing, China. E-mail: thomas.frauenheim@bccms.uni-bremen.de*

[e]*Shenzhen JL Computational Science and Applied Research Institute, 518110 Shenzhen, China. E-mail: thomas.frauenheim@bccms.uni-bremen.de*

† Electronic supplementary information (ESI) available. See DOI: 10.1039/d1ra06010d

devices.[29–31] It was also shown that sulfur line vacancies in MoS_2 can behave like pseudo-ballistic wire for electron transport.[32]

So far, several theoretical studies have reported the transport properties of phase-engineered devices based on TMDs monolayers including MoS_2 based lateral junctions.[11,12,33–35,35–37] In most of these studies, however, it is assumed that two phases have a perfect crystalline structure and connected *via* an atomically sharp and defect-free interface.

Here, transport properties of devices based on MLs MoS_2, containing various point vacancies and antisites at the interface between metallic and semiconducting phases, are the subject of the present study. Our systematic investigations show significant improvements in the current, as molybdenum vacancy and vacancy complexes are created at the interfaces of two phases. These findings render defect engineering as an efficient route to further improve the performance of the devices based on the lateral heterojunctions formed from TMDs.

1. Computational details

Density-functional theory (DFT) calculations were performed using numerical atomic orbitals (NAOs) basis sets as implemented in SIESTA code.[38,39] The norm-conserving pseudopotentials, including the effect of core electrons, are employed, which were obtained using the Troullier–Martin method.[40,41] The Perdew–Burke–Ernzerhof (PBE) functional in the generalized gradient approximation (GGA) is used to describe the exchange and correlation interactions.[42]

In the optimization calculations, the Brillouin zone (BZ) of supercells was sampled using a $9 \times 1 \times 3$ Monkhorst–Pack grid. In the electronic and transport calculations, 5 and 29 *k*-points were used, respectively, along the transverse direction. The conjugate-gradients (CG) method was applied to optimize the lattice vectors and atomic positions of all the structures and interfaces. The geometries were considered relaxed when the Hellman–Feynman forces on each atom became smaller than 10 meV $Å^{-1}$. The energy cut-off of 450 Ry is used in the framework of the real-space grid techniques to obtain Hartree, exchange, and correlation energies. The Split-Norm was set to 0.16 and the Energy-Shift of 0.02 Ry was chosen to determine the confinement radii. The total energy convergency criteria (ΔE_{tot}) is chosen to be 10^{-5} eV for *k*-points and 10^{-4} eV for energy cut-off. When the difference between two consecutive steps was less than 10^{-4} eV, the total energies in self-consistent field (SCF) cycles were considered converging.

The electron transport calculations were performed using non-equilibrium Green's functions (NEGF) techniques, as implemented in TranSIESTA and TBtrans.[43,44] The same basis sets as for the electronic calculations, namely SZP, were employed for the transport calculations. The current through the heterophase junction under a finite bias voltage was calculated within the Landauer formula:[45]

$$I = \frac{2e}{h}\int \mathrm{Trace}\left[G_C^{\dagger}(E)\Gamma_R(E)G_C(E)\Gamma_L(E)\right](f_L(E) - f_R(E))\mathrm{d}E. \quad (1)$$

where $G_C^{\dagger}(E)$ and $G_C(E)$ are the retarded and advanced Green's functions of the channel region. The effect of left (L) and right (R) electrodes are projected onto the scattering region *via* their corresponding self-energies, $\Gamma_L(E)$ and $\Gamma_R(E)$. The Fermi distribution of $f_L(E)$ and $f_R(E)$ represent the available states for electrons in the left and right electrodes. In order to calculate the self-energies of the electrodes, we have used 65 *k*-points along the transport direction (*Z*-axis) and 5 *k*-points transverse to the transport direction (*X*-axis) to simulate semi-infinite metallic electrodes. The transport calculations were performed at 300 K.

2. Results and discussion

Depending on the edge orientation of monolayers, armchair and zigzag interfaces can be realized. The armchair interfaces have been shown to be most stable against buckling.[11,34] They are also energetically more favorable than connecting the zigzag terminated edges in the sulfur-rich limit.[33,34] The recent theoretical study showed that the conductivity of the armchair edges is higher than the zigzag interfaces due to the presence of metallic Mo zigzag chains along the transport direction.[11] Accordingly, we consider the armchair interface in the present study. In order to create Schottky contacts at the interfaces, the semiconducting 2H-phase of MoS_2 (channel region) is sandwiched between two metal electrodes of 1T-MoS_2, as shown in Fig. 1.

The size of the whole device is 117.50 Å along the transport direction (*Z* axis) and 22.00 Å in the transverse direction (*X* axis), including the channel with a length of 98.46 Å corresponding to 31 unit cells of MoS_2. The channel length is long enough to avoid artificial interactions between the two electrodes. Also, it includes small adjacent portions of the 1T phase as buffer layers to provide a computationally convenient configuration for calculating self-energies at the boundaries.[46] The periodic boundary conditions were applied along the axis transverse to the transport direction. A vacuum layer of 50 Å normal to the monolayers was considered, which prevents interactions between adjacent supercells.

Several junctions composed of 1T and 2H of MLs MoS_2 are considered without defects (perfect) and when containing point defects in the phase boundaries, as shown in Fig. 1. Here, we considered only the high-symmetry cases where similar defects are created at both interfaces. In Fig. S1 of the ESI,† the structure of the whole device is shown. We considere 10 types of point defects, most of which were observed in experiments[16,17,19,20,47,48] and their stability were analyzed by DFT calculations.[15,27,28,49] Our main objective is to present the difference between the effect of such defects in transport properties of 1H pristine phases and 1T–2H heterostructures. Hence, complex defects containing antisite aggregated with another type of defect, as mentioned in ref. 50, are neglected in this study. We look at a sulfur and a molybdenum vacancy, V_S and V_{Mo}, a double sulfur vacancy from upper and bottom layers V_{2S-top}, and the case of removing two atoms from the upper sulfur layer and parallel to the interface, V_{2S-par}. Besides, vacancy complexes of molybdenum and three sulfurs (V_{Mo+3S}) and six sulfurs (V_{Mo+6S}) are also studied. Four antisites are also considered: Mo_S, Mo_{2S-top}, S_{Mo}, and $2S - top_{Mo}$. In this study,

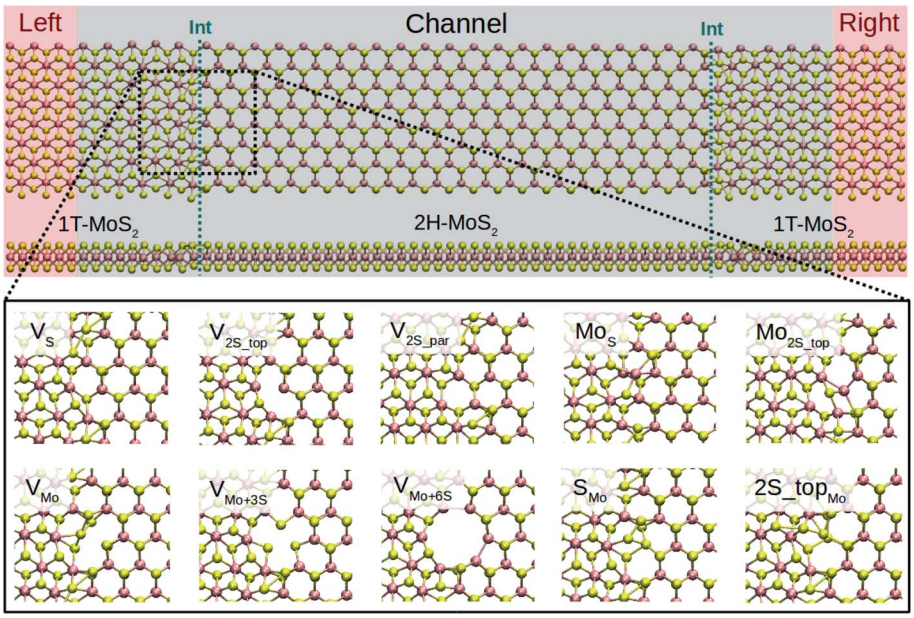

Fig. 1 (Upper) Schematic of the T–H heterophase junction of MoS_2 monolayer. Electrodes (only 1T-MoS_2) and channel region (a combination of 1T- and 2H-MoS_2) are highlighted with shaded red and black, respectively. The interfaces are indicated with green dashed-lines. (Lower) Optimized structures of the point defects at the left interface of the devices are shown. Only defects at the left electrode are shown here. The complete devices are shown in Fig. S1 in the ESI.†

all defects are assumed to be in their charge-neutral states. The previous report on the charged defects in semiconducting 2H-MoS_2 revealed that both V_S and V_{Mo} are likely to assume negative charge states, when the system has n-type doping[49] character. However, because of the metallic character of 1T-MoS_2, defects in the 1T–2H heterophase junction are considered only in their neutral state as the extra charge migrates to the 1T phase.

Our electronic structure calculations indicate that 2H-MoS_2 is a semiconductor with a bandgap of 1.73 eV, while 1T-MoS_2 has a metallic character (see Fig. S2†). We have compared our calculated band gap with the values reported at different levels of theories, as listed in Table S1.† Our result is in good agreement with previous theoretical reports at the same level of theory.[6,49,51–53] In the case of defective systems, it has been known that more advanced methods like GW approximation would only lead to shifts in the band edges and defect levels in the same direction, but do not change the qualitative picture of the defect states within the bandgap and their relative position to the VBM and CBM (see ref. 54–56). Therefore, it is expected that these methods would only affect the range of the applied voltage and the provided analysis remain intact.

The previous theoretical studies have shown no difference or a difference of 0.63% between the lattice constant of the T- and H-phase of MoS_2 monolayers.[6,49,51–53] Therefore, the same lattice parameters, namely 3.176 Å, are used for both phases. Such a phase transition can be seen as the collective displacement of sulfur atoms while the stoichiometry of the materials is preserved. The constructed lateral heterostructures with armchair edges are optimized, as shown at the top of Fig. 1. It should be noted that the optimization could not transform 1T into the 2H phase but induce some distortions, indicating the activation barrier for the phase transformation is higher than the relaxation of the boundary. In addition, the atomic network can be subjected to strain as a result of defects in the phase boundary. Fig. S3† shows the strain map, which is specified as the total displacements in all three axes as compared to the perfect interface. It can be seen that the largest change in the atomic positions occurs in the case of V_{Mo+3S} at the interfaces while the sulfur vacancies induce the smallest displacements into the phase boundary.

2.1. Sulfur vacancies

In this section, we present the electronic and transport properties of T–H heterophase junction containing interfacial sulfur vacancies; V_S, V_{2S-top}, and V_{2S-par}. In Fig. 2, local density of

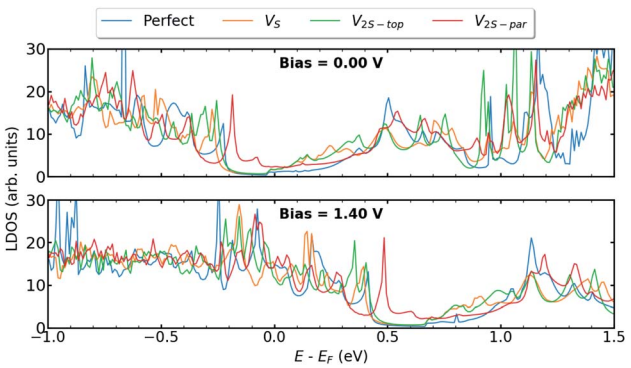

Fig. 2 LDOS at the left interface of T–H heterophase junction containing various sulfur vacancies; V_S, V_{2S-top}, and V_{2S-par}. Energies are shifted with respect to their corresponding Fermi energy.

states (LDOS) on the atoms at the left interface of such devices are plotted at bias = 0.00 V and bias = 1.40 V. In the following, the term "interface" is used for a part of the device, which consists of atoms from one layer of 1T-MoS_2 and one layer of 2H-MoS_2. Due to the electronic states from the 1T phase, the band gap in LDOS is narrower than that for the pristine 2H phase of MoS_2. Comparing the two figures, there is a shift in the energy, corresponding to half of the applied voltage.

The presence of defects introduces new states close to the Fermi level and increases electron density at the interface, which is mainly contributed by metal d orbitals. It is evident that defect-associated states are more pronounced in the case of V_{2S-par} where the electron density is enhanced in the vicinity of the Fermi level, including a peak at −0.2 eV. The results showed that other types of sulfur vacancies have a negligible impact on the electronic structure around the Fermi energy. It should be noted that the sulfur vacancies in 2H-MoS_2 monolayers act as scattering centers and consequently diminish the transport properties.[25–28]

In order to elaborate the electron conduction dependency on the geometry of contact between the T and the H phases, transmission spectra for the junction without and with interfacial defects at two bias, 0.00 V and 1.40 V, are shown in Fig. 3a and b, respectively. Corresponding to the band gap of 2H-MoS_2, there is no transmission at zero bias within an energy range of 1.7 eV around the Fermi level. A comparison between the perfect interface and those containing sulfur vacancies indicates an increase in transmission probability, suggesting the contribution of defect states in electrical transport. Specifically, the transmission coefficients close to the valence band edge can be increased to almost two times for the case of V_{2S-par} vacancy. The *I*–*V* characteristics of the studied T–H heterophase junction are shown in Fig. 3c. The junction displays a non-linear current–voltage similar to the characteristics of a resonant tunneling diode. The energy mismatch between the Fermi energy of the metallic 1T electrodes and the lowest unoccupied levels of the 2H phase causes the presence of zero current and the need for threshold voltage to produce finite current flow through the junction. The value of threshold voltage was reduced from 1.0 V for the perfect interface to 0.75 V for the interface with divacancy. The appearance of defect-associated resonant states in the transmission spectra within the voltage window changes the current through the system, leading to an increase by an order of magnitude, when V_{2S-par} vacancy is present at the interfaces, as shown in Fig. 3c.

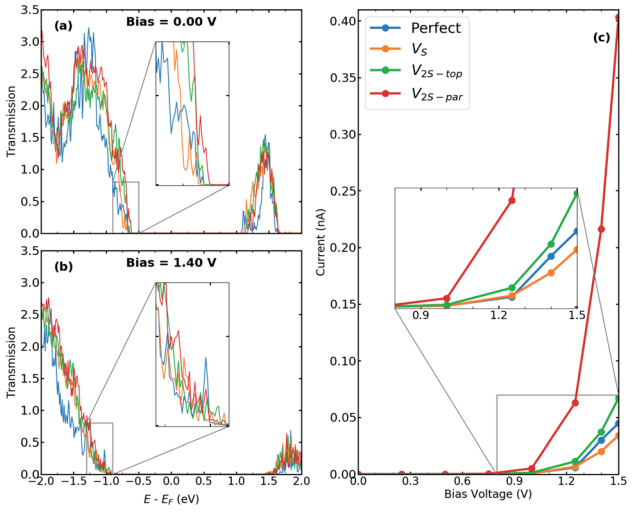

Fig. 3 Transmission spectra for T–H heterophase junction of MoS_2 monolayer containing various sulfur vacancies at both interfaces at (a) bias = 0.00 V and (b) bias = 1.40 V. Energies are shifted with respect to their corresponding Fermi energy. The insets show the change in the electronic transmission channels at the top of the valence band. (c) *I*–*V* characteristics for the same devices. The inset shows the current around the threshold voltage.

2.2. Molybdenum vacancies and vacancy complexes

We calculate the electronic and transport properties of the T–H heterophase junction when molybdenum vacancy, V_{Mo}, and vacancy complexes V_{Mo+3S} and V_{Mo+6S} are present at the interface. The LDOS of the interface is shown in Fig. 4 at bias = 0.00 V and bias = 1.40 V. Here, the applied bias has shifted the energies. The electronic structure of the interfaces with a single Mo vacancy varies more than that of a single sulfur vacancy. In the case of larger point defects, *i.e.* V_{Mo+6S}, the electronic structure shows several resonant states around the Fermi level which are mainly formed by Mo 4d states. The defect-induced changes in the electronic structure affect the carrier injection through the junction. The transmission function (Fig. 5a and b) at the top of the valence band shows a significant enhancement when vacancies are introduced into the interfaces. Accordingly, the current is increased by up to three orders of magnitude in comparison to the perfect interface. This is due to an enhancement of carrier occupations near the Fermi level, which leads to an increase in the transmission spectrum. The projected local density of states (Fig. S6†) also indicates more electronic states at the interface with Mo vacancy, generating a strong electron transmission at energies around −0.5 eV. This leads to an increase in the electron conduction within the corresponding bias window (Fig. 5c). A similar effect was recently reported on the dependence of transmission on the geometry of

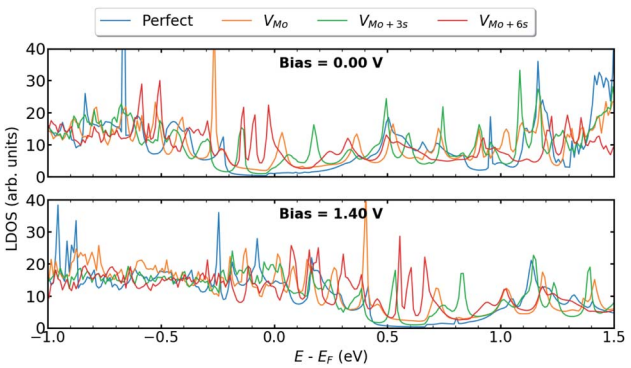

Fig. 4 LDOS at the left interface of T–H heterophase junction containing molybdenum vacancy, V_{Mo}, and vacancy complexes as V_{Mo+3S} and V_{Mo+6S}. Energies are shifted with respect to their corresponding Fermi energy.

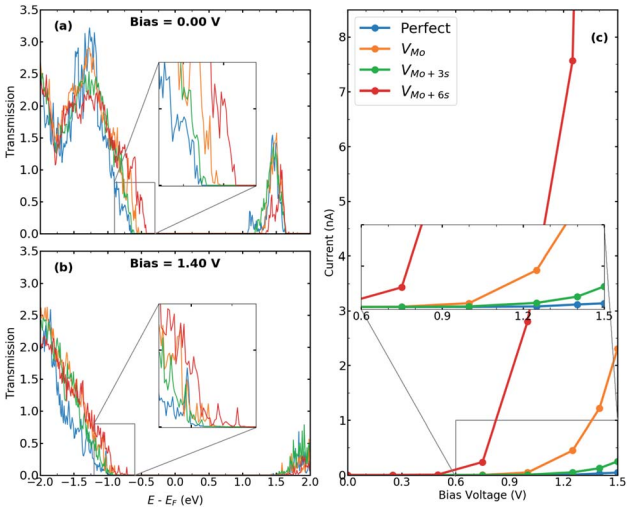

Fig. 5 Transmission spectra for T–H heterophase junction of MoS_2 monolayer containing molybdenum vacancy, V_{Mo}, and vacancy complexes as V_{Mo+3S} and V_{Mo+6S} at both interfaces at (a) bias = 0.00 V and (b) bias = 1.40 V. Energies are shifted with respect to their corresponding Fermi energy. The insets show the change in the electronic transmission channels at the top of the valence band. (c) *I*–*V* characteristics for the same devices. The inset shows the current around the threshold voltage.

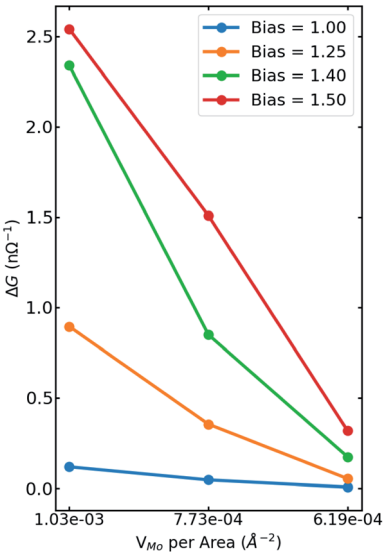

Fig. 6 Difference in the conductance through perfect systems and device with V_{Mo} ($\Delta G = G_{defect} - G_{perfect}$) as a function of the device's area at different bias voltages. Since the number of vacancies is the same for all cases, it is also a function of the defect density. It is true that more transport channels are added to wider devices, however, at the same time defect density is reduced, hence, decreasing the current through defective devices. Thus, the change in conductance is approaching zero, as the system gets wider.

interface in monolayer based heterojunctions.[57,58] The interfaces with V_{Mo+6S} vacancy demonstrate a threshold voltage of $\approx$0.5 V, half of that for a perfect interface.

To further investigate the transport behaviour at the interface, we also plot the vector current for perfect systems and devices with V_{Mo} at both interfaces (Fig. S4†). Vector current displays the direction and the amount of current, coming from the left or right electrode, projected on each atom and at a specific energy channel. While the perfect interface shows dominant current scattering at the T–H boundary for low bias voltages, *e.g.* $V = -0.5$ V, the currents are delocalized in the channel region with V_{Mo} at the interface, suggesting that electrons have been well transmitted from electrodes to the channel region.

We have also studied the influence of defect concentrations on the transport properties through the interfaces. Here, we fixed the length of the channel but varied its width, including the interfaces with a single V_{Mo}. Fig. 6 shows the difference in the conductance through devices ($\Delta G = G_{defect} - G_{perfect}$) as a function of the devices' areas. It is evident that the conductance reduces with decreasing the defect concentration approaching the value of the perfect interface for zero-defect density. Variation of channel widths has two different effects on the transport properties: on one hand, the number of transport channels increases with the width of the channel. On the other hand, for a constant number of defect sites, increasing the channel width leads to a decrease in the carrier densities around the Fermi level. The former effect is canceled out by subtracting the conductivity of the system from the corresponding one with the pristine interface. As a result, for wider channels (lower concentrations), the increase in electrical conductivity is linearly reduced.

2.3. Antisites

Because vacancy and antisite are both high electron-scattering centers, their presence in TMDs can impair sample mobility.[59] We further investigate the influence of antisites defects, such as Mo_S, Mo_{2S-top}, S_{Mo}, and $2S - top_{Mo}$, at the interfaces of T–H heterophase junctions. Among all the considered antisites, the situation where molybdenum vacancy is substituted with two sulfurs ($2S - top_{Mo}$) provides the most pronounced defect associated states at the valence band edge (Fig. 7). When compared with the Mo vacancy, the defect states are more localized and originated mainly from hybridization between the Mo_d–S_p orbitals. The contributing orbitals to the LDOS at the left interface are shown in Fig. S5 in the ESI.†

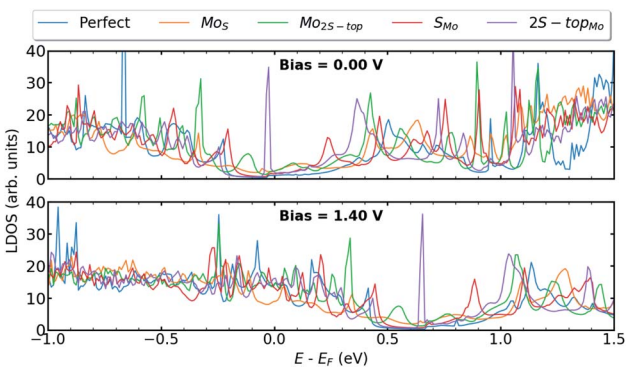

Fig. 7 LDOS at the left interface of T–H heterophase junction containing various substitutions; Mo_S, Mo_{2S-top}, S_{Mo}, $2S - top_{Mo}$. Energies are shifted with respect to their corresponding Fermi energy.

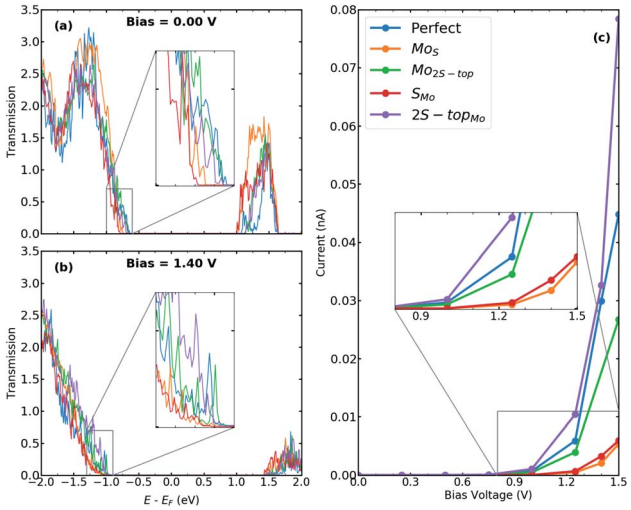

Fig. 8 Transmission spectra for T–H heterophase junction of MoS_2 monolayer containing various substitutions; Mo_S, Mo_{2S-top}, S_{Mo}, $2S - top_{Mo}$, at both interfaces at (a) bias = 0.00 V and (b) bias = 1.40 V. Energies are shifted with respect to their corresponding Fermi energy. The insets show the change in the electronic transmission channels at the top of the valence band. (c) *I–V* characteristics for the same devices. The inset shows the current around the threshold voltage.

In Fig. 8a and b, transmission spectra for phase-engineered devices based on MLs MoS_2, containing various substitutions, are displayed at bias = 0.00 & 1.40 V. Fig. 8c shows the corresponding *I–V* characteristics as a function of bias voltages up to 1.50 V. When vacancies are substituted with sulfur or molybdenum atoms, the current stays in the same order as for the device with perfect interfaces. Only for the case of $2S - top_{Mo}$, the current has been slightly increased due to the presence of midgap defect states observed in LDOS and the enhancement in the transmission probabilities. It's also worth noting that, in contrast to the case of perfect interfaces, the presence of antisite defects inevitably results in more phonon scattering channels, which may be beneficial in lowering lattice thermal conductivity.

3. Conclusions

In the present paper, the transport properties of charge carriers through devices based on metallic (1T) and semiconductor (2H) phases of MoS_2 monolayers are investigated. Various point defects are present at both interfaces: V_S, V_{2S-top}, V_{2S-par}, V_{Mo}, V_{Mo+3S}, V_{Mo+6S}, Mo_S, Mo_{2S-top}, S_{Mo}, and $2S - top_{Mo}$. The first-principles simulations and NEGF technique are used to compute the LDOS, transmission curves, and *I–V* characteristics of perfect and defective devices under bias in the range of 0.00 V till 1.50 V. Our systematic study shows that defects at the interfaces provide the opportunity for further improvement of the transport properties of such devices. More notably, we found that transport properties are enhanced in the presence of energetically favorable intrinsic point defects. In contrast to the scattering character of defects in 2H-phase MoS_2, at the interface, they lead to the emergence of resonant states close to the Fermi level, thereby giving rise to the enhancement of the current flow. In particular, creating a molybdenum vacancy induces defect midgap states in the LDOS and improves the transport characteristics, which, in turn, leads to an increase in the current up to two orders of magnitude. The knowledge developed in this study could pave the way for the promising applications of lateral heterojunctions of 1T-2H MoS_2 monolayers in electronic devices.

Author contributions

Conceptualization, M. B. and M. G.-A; investigation, M. B.; methodology, M. B., and M. G.-A.; writing, M. B., M. G.-A., T. F.; supervision, M. G.-A, T. F. All authors have read and agreed to the published version of the manuscript.

Conflicts of interest

There are no conflicts to declare.

Acknowledgements

We thank the DFG funded research training group "GRK 2247".M. B. acknowledges the support provided by DAAD and the PIP program at Bremen University. M. B. also thanks Dr Nick Papior for his support during the transport calculations and Dr Miguel Pruneda for his help to produce well-performed basis-sets and pseudopotentials.

Notes and references

1 O. Ávalos-Ovando, D. Mastrogiuseppe and S. E. Ulloa, *J. Phys.: Condens. Matter*, 2019, **31**, 213001.
2 J. Wang, Z. Li, H. Chen, G. Deng and X. Niu, *Nano-Micro Lett.*, 2019, **11**, 3.
3 M. Houssa, R. Meng, V. Afanas'ev and A. Stesmans, *Appl. Sci.*, 2020, **10**, 2731.
4 M. Chhowalla, H. S. Shin, G. Eda, L. J. Li, K. P. Loh and H. Zhang, *Nat. Chem.*, 2013, **5**, 263–275.
5 A. Nourbakhsh, A. Zubair, R. N. Sajjad, T. K. Amir, W. Chen, S. Fang, X. Ling, J. Kong, M. S. Dresselhaus, E. Kaxiras, K. K. Berggren, D. Antoniadis and T. Palacios, *Nano Lett.*, 2016, **16**, 7798–7806.
6 D. Marian, E. Dib, T. Cusati, A. Fortunelli, G. Iannaccone and G. Fiori, *Technical Digest – International Electron Devices Meeting (IEDM)*, 2017, pp. 14.1.1–14.1.4.
7 Y. C. Lin, D. O. Dumcenco, Y. S. Huang and K. Suenaga, *Nat. Nanotechnol.*, 2014, **9**, 391–396.
8 R. Kappera, D. Voiry, S. E. Yalcin, B. Branch, G. Gupta, A. D. Mohite and M. Chhowalla, *Nat. Mater.*, 2014, **13**, 1128–1134.
9 S. Cho, S. Kim, J. H. Kim, J. Zhao, J. Seok, D. H. Keum, J. Baik, D. H. Choe, K. J. Chang, K. Suenaga, S. W. Kim, Y. H. Lee and H. Yang, *Science*, 2015, **349**, 625–628.
10 J. Kang, W. Liu, D. Sarkar, D. Jena and K. Banerjee, *Phys. Rev. X*, 2014, **4**, 031005.

11 Y. Aierken, C. Sevik, O. Gülseren, F. M. Peeters and D. Çakir, *Nanotechnology*, 2018, **29**, 295202.
12 Z. Q. Fan, X. W. Jiang, J. Chen and J. W. Luo, *ACS Appl. Mater. Interfaces*, 2018, **10**, 19271–19277.
13 X. Zhang, Z. Jin, L. Wang, J. A. Hachtel, E. Villarreal, Z. Wang, T. Ha, Y. Nakanishi, C. S. Tiwary, J. Lai, L. Dong, J. Yang, R. Vajtai, E. Ringe, J. C. Idrobo, B. I. Yakobson, J. Lou, V. Gambin, R. Koltun and P. M. Ajayan, *ACS Appl. Mater. Interfaces*, 2019, **11**, 12777–12785.
14 A. L. Friedman, F. K. Perkins, A. T. Hanbicki, J. C. Culbertson and P. M. Campbell, *Nanoscale*, 2016, **8**, 11445–11453.
15 H.-P. Komsa, S. Kurasch, O. Lehtinen, U. Kaiser and A. V. Krasheninnikov, *Phys. Rev. B: Condens. Matter Mater. Phys.*, 2013, **88**, 035301.
16 X. Yang, Q. Li, G. Hu, Z. Wang, Z. Yang, X. Liu, M. Dong and C. Pan, *Sci. China Mater.*, 2016, **59**, 182–190.
17 S. W. Han, Y. Park, Y. H. Hwang, S. Jekal, M. Kang, W. G. Lee, W. Yang, G. D. Lee and S. C. Hong, *Sci. Rep.*, 2016, **6**, 1–8.
18 M. Ghorbani-Asl, S. Kretschmer, D. E. Spearot and A. V. Krasheninnikov, *2D Materials*, 2017, **4**, 025078.
19 L. Ma, Y. Tan, M. Ghorbani-Asl, R. Boettger, S. Kretschmer, S. Zhou, Z. Huang, A. V. Krasheninnikov and F. Chen, *Nanoscale*, 2017, **9**, 11027–11034.
20 J. Klein, M. Lorke, M. Florian, F. Sigger, L. Sigl, S. Rey, J. Wierzbowski, J. Cerne, K. Müller, E. Mitterreiter, P. Zimmermann, T. Taniguchi, K. Watanabe, U. Wurstbauer, M. Kaniber, M. Knap, R. Schmidt, J. J. Finley and A. W. Holleitner, *Nat. Commun.*, 2019, **10**, 2755.
21 K. Barthelmi, J. Klein, A. Hötger, L. Sigl, F. Sigger, E. Mitterreiter, S. Rey, S. Gyger, M. Lorke, M. Florian, F. Jahnke, T. Taniguchi, K. Watanabe, V. Zwiller, K. D. Jöns, U. Wurstbauer, C. Kastl, A. Weber-Bargioni, J. J. Finley, K. Müller and A. W. Holleitner, *Appl. Phys. Lett.*, 2020, **117**, 070501.
22 E. Mitterreiter, B. Schuler, A. Micevic, D. Hernangómez-Pérez, K. Barthelmi, K. A. Cochrane, J. Kiemle, F. Sigger, J. Klein, E. Wong, E. S. Barnard, K. Watanabe, T. Taniguchi, M. Lorke, F. Jahnke, J. J. Finley, A. M. Schwartzberg, D. Y. Qiu, S. Refaely-Abramson, A. W. Holleitner, A. Weber-Bargioni and C. Kastl, *Nat. Commun.*, 2021, **12**, 3822.
23 S. Kretschmer, H. P. Komsa, P. Bøggild and A. V. Krasheninnikov, *J. Phys. Chem. Lett.*, 2017, **8**, 3061–3067.
24 J. Zhu, Z. Wang, H. Yu, N. Li, J. Zhang, J. Meng, M. Liao, J. Zhao, X. Lu, L. Du, R. Yang, D. Shi, Y. Jiang and G. Zhang, *J. Am. Chem. Soc.*, 2017, **139**, 10216–10219.
25 M. Ghorbani-Asl, A. N. Enyashin, A. Kuc, G. Seifert and T. Heine, *Phys. Rev. B: Condens. Matter Mater. Phys.*, 2013, **88**, 245440.
26 M. Pandey, F. A. Rasmussen, K. Kuhar, T. Olsen, K. W. Jacobsen and K. S. Thygesen, *Nano Lett.*, 2016, **16**, 2234–2239.
27 Z. Lin, B. R. Carvalho, E. Kahn, R. Lv, R. Rao, H. Terrones, M. A. Pimenta and M. Terrones, *2D Materials*, 2016, **3**, 022002.
28 M. Bahmani, M. Faghihnasiri, M. Lorke, A. B. Kuc and T. Frauenheim, *Phys. Status Solidi B*, 2020, 1900541.
29 K. S. Novoselov, D. Jiang, F. Schedin, T. J. Booth, V. V. Khotkevich, S. V. Morozov and A. K. Geim, *Proc. Natl. Acad. Sci. U. S. A.*, 2005, **102**, 10451–10453.
30 B. Radisavljevic, A. Radenovic, J. Brivio, V. Giacometti and A. Kis, *Nat. Nanotechnol.*, 2011, **6**, 147–150.
31 Y. H. Lee, X. Q. Zhang, W. Zhang, M. T. Chang, C. T. Lin, K. D. Chang, Y. C. Yu, J. T. W. Wang, C. S. Chang, L. J. Li and T. W. Lin, *Adv. Mater.*, 2012, **24**, 2320–2325.
32 K. S. Yong, D. M. Otalvaro, I. Duchemin, M. Saeys and C. Joachim, *Phys. Rev. B: Condens. Matter Mater. Phys.*, 2008, **77**, 205429.
33 Z. Hu, S. Zhang, Y. N. Zhang, D. Wang, H. Zeng and L. M. Liu, *Phys. Chem. Chem. Phys.*, 2015, **17**, 1099–1105.
34 G. Sivaraman, F. A. De Souza, R. G. Amorim, W. L. Scopel, M. Fyta and R. H. Scheicher, *J. Phys. Chem. C*, 2016, **120**, 23389–23396.
35 Y. An, M. Zhang, D. Wu, Z. Fu and K. Wang, *J. Mater. Chem. C*, 2016, **4**, 10962–10966.
36 Z. Q. Fan, X. W. Jiang, J. W. Luo, L. Y. Jiao, R. Huang, S. S. Li and L. W. Wang, *Phys. Rev. B*, 2017, **96**, 165402.
37 D. Marian, E. Dib, T. Cusati, E. G. Marin, A. Fortunelli, G. Iannaccone and G. Fiori, *Phys. Rev. Appl.*, 2017, **8**, 054047.
38 P. Ordejon, E. Artacho and J. M. Soler, *Phys. Rev. B: Condens. Matter Mater. Phys.*, 1996, **53**, R10441–R10444.
39 J. M. Soler, E. Artacho, J. D. Gale, A. García, J. Junquera, P. Ordejón and D. Sánchez-Portal, *J. Phys.: Condens. Matter*, 2002, **14**, 2745–2779.
40 N. Troullier and J. L. Martins, *Phys. Rev. B: Condens. Matter Mater. Phys.*, 1991, **43**, 1993–2006.
41 N. Troullier and J. L. Martins, *Phys. Rev. B: Condens. Matter Mater. Phys.*, 1991, **43**, 8861–8869.
42 J. P. Perdew, K. Burke and M. Ernzerhof, *Phys. Rev. Lett.*, 1996, **77**, 3865–3868.
43 M. Brandbyge, J. L. Mozos, P. Ordejón, J. Taylor and K. Stokbro, *Phys. Rev. B: Condens. Matter Mater. Phys.*, 2002, **65**, 1654011–16540117.
44 N. Papior, N. Lorente, T. Frederiksen, A. García and M. Brandbyge, *Comput. Phys. Commun.*, 2017, **212**, 8–24.
45 R. Landauer, *Philos. Mag.*, 1970, **21**, 863–867.
46 M. Ghorbani-Asl, P. D. Bristowe and K. Koziol, *Phys. Chem. Chem. Phys.*, 2015, **17**, 18273–18277.
47 W. Zhou, X. Zou, S. Najmaei, Z. Liu, Y. Shi, J. Kong, J. Lou, P. M. Ajayan, B. I. Yakobson and J. C. Idrobo, *Nano Lett.*, 2013, **13**, 2615–2622.
48 M. G. Stanford, Y.-C. Lin, M. G. Sales, A. N. Hoffman, C. T. Nelson, K. Xiao, S. McDonnell and P. D. Rack, *npj 2D Mater. Appl.*, 2019, **3**, 13.
49 H.-P. Komsa and A. V. Krasheninnikov, *Phys. Rev. B: Condens. Matter Mater. Phys.*, 2015, **91**, 125304.
50 F. Aryeetey, T. Ignatova and S. Aravamudhan, *RSC Adv.*, 2020, **10**, 22996–23001.
51 R. Roldán, J. A. Silva-Guillén, M. P. López-Sancho, F. Guinea, E. Cappelluti and P. Ordejón, *Ann. Phys.*, 2014, **526**, 347–357.
52 D. Saha and S. Mahapatra, *Appl. Phys. Lett.*, 2016, **108**, 253106.

53 C. H. Sharma, A. P. Surendran, A. Varghese and M. Thalakulam, *Sci. Rep.*, 2018, **8**, 12463.
54 M. H. Naik and M. Jain, *Phys. Rev. Mater.*, 2018, **2**, 084002.
55 S. Refaely-Abramson, D. Y. Qiu, S. G. Louie and J. B. Neaton, *Phys. Rev. Lett.*, 2018, **121**, 167402.
56 B. Schuler, D. Y. Qiu, S. Refaely-Abramson, C. Kastl, C. T. Chen, S. Barja, R. J. Koch, D. F. Ogletree, S. Aloni, A. M. Schwartzberg, J. B. Neaton, S. G. Louie and A. Weber-Bargioni, *Phys. Rev. Lett.*, 2019, **123**, 076801.
57 Y. An, Y. Hou, K. Wang, S. Gong, C. Ma, C. Zhao, T. Wang, Z. Jiao, H. Wang and R. Wu, *Adv. Funct. Mater.*, 2020, **30**, 2002939.
58 Y. An, K. Wang, S. Gong, Y. Hou, C. Ma, M. Zhu, C. Zhao, T. Wang, S. Ma, H. Wang, R. Wu and W. Liu, *npj Comput. Mater.*, 2021, **7**, 45.
59 J. Hong, Z. Hu, M. Probert, K. Li, D. Lv, X. Yang, L. Gu, N. Mao, Q. Feng, L. Xie, J. Zhang, D. Wu, Z. Zhang, C. Jin, W. Ji, X. Zhang, J. Yuan and Z. Zhang, *Nat. Commun.*, 2015, **6**, 6293.